Metal-insulator transition in single crystalline ZnO nanowires

Metal-insulator transition in single crystalline ZnO nanowires

G. Milano[1,2*], L. D'Ortenzi[1], K. Bejtka[3], B. Ciubini[2], S. Porro[2], L. Boarino[1], C. Ricciardi[2*]

[1] Advanced Materials Metrology and Life Science Division, INRiM (Istituto Nazionale di Ricerca Metrologica), Strada delle Cacce 91, 10135, Torino, Italy.
[2] Department of Applied Science and Technology, Politecnico di Torino, c.so Duca degli Abruzzi 24, I-10129 Torino, Italy
[3] Center for Sustainable Future Technologies, Istituto Italiano di Tecnologia, c.so Trento 21, I-10129 Torino, Italy

* E-mail: g.milano@inrim.it, carlo.ricciardi@polito.it

Received xxxxxx
Accepted for publication xxxxxx
Published xxxxxx

Abstract

In this work, we report on the metal-insulator transition and electronic transport properties of single crystalline ZnO nanowires synthetized by means of Chemical Vapor Deposition. As revealed by temperature-dependent measurements, the electronic transport mechanism in these nanostructures is in good agreement with the presence of two thermally activated conduction channels. Moreover, it was observed that the electrical properties of ZnO NWs can be tuned from semiconducting to metallic-like as a function of temperature, since a metal-to-insulator transition (MIT) was observed at a critical temperature of ~365 K. Results evidenced that the peculiar electronic transport properties of ZnO NWs are related to the high intrinsic *n*-type doping of these nanostructures that is responsible, at room temperature, of a charge carrier density that lays just below the critical concentration for the metal-to-insulator transition.

Keywords: nanowires, zinc oxide, metal-insulator transition, field-effect transistor

1. Introduction

Among nanostructures, ZnO nanowires (NWs) have attracted great interest because of the easiness of fabrication and outstanding photonic, plasmonic, piezoelectric and mechanical properties [1–5]. In addition, the electronic properties of these nanostructures make ZnO NWs good candidates as building blocks for a NW-based electronics, finding application as nano-sensors [6,7], field effect transistors (FET) [8,9], photodetectors [10] and resistive switching/memristive devices where ionics is coupled to electronics [11–16]**.** As a consequence of the presence of shallow donor levels below the conduction band edge, ZnO is usually an unintentionally-doped *n*-type semiconductor [17]. Depending on the temperature range, several conduction mechanisms have been proposed to match experimental results on ZnO NW conductivity, such as thermally activated conduction mechanism [18–20], nearest-neighbour hopping [18,19], fluctuation induced tunnelling conductance (FITC) [20] and variable-range hopping conduction [21]. The wide range of conduction mechanisms reported can be related to different material characteristics such as structural properties, material defectivity and intrinsic doping. Importantly, the doping level of the material is a key aspect that regulates the metal-to-insulator transition (MIT) in metal-oxide semiconductors, where a crossover in between the insulator state and a metallic state is observed above a critical carrier concentration [22,23]. Even if MITs have been investigated in

a wide range of materials over the past 40 years[24], only few works reported this transition in natively doped ZnO nanostructures. In these works, the MIT was observed below room temperature [25] or was induced by UV illumination [26].

In this work, we show that the electronic transport properties of single crystalline ZnO NWs are characterized by two thermally activated conduction channels and a metal-to-insulator transition just above room temperature ($T_c \sim 365$ K), that was observable without any external stimuli. Results show that the peculiar conduction mechanism observed can be attributed to the high intrinsic doping of these nanostructures that, at room temperature, have a charge carrier concentration that lays just below the critical concentration for the metal-to-insulator transition.

2. Experimental section

2.1 Synthesis and characterization

ZnO NWs were grown by Low Pressure Chemical Vapour Deposition (LP-CVD) in a quartz tube furnace, following the procedure adopted in previous works [11,27]. A Pt substrate, placed inside the quartz tube on an alumina boat, acts as a catalyst. The Pt substrate with thickness of 100 nm was realized by sputtering on a SiO_2/Si wafer, using Ta (20 nm) as adhesion layer. A Zn foil (purity 99.99%) was placed close to the substrate and was used as Zn source. After that the chamber was placed in vacuum, a heating step was performed with a ramp rate of 8.6 °C/min by fluxing Ar (60 sccm from ambient temperature up to 300°C, 300 sccm from 300°C up to 650°C). Subsequently, the temperature was fixed at 650°C for 20 min while 200 sccm of O_2 and 300 sccm of Ar were fluxed into the chamber. During this growth step, the pressure was 1.4 Torr. The morphology of as grown ZnO NWs was investigated by means of Field Emission Scanning Electron Microscopy (FE-SEM), using a Zeiss Merlin. Transmission Electron Microscopy (TEM) was performed by means of a FEI Tecnai F20ST equipped with a field emission gun (FEG) that operates at 200 kV. The sample preparation for TEM measurements consisted in the dispersion of ZnO NWs from the growth substrate to the TEM grid with a mounted hair, without exposing NWs to any solvent. Photoluminescence measurements were performed on as grown ZnO NW arrays with an excitation source of 345 nm at room temperature, using a Horiba Fluorolog spectrometer.

2.2 Device fabrication and electrical characterization

The fabrication of single ZnO NW devices required combined optical and electron beam lithographies (EBL), using a similar procedure than the one reported in our previous works [12,13]. In brief, NW-based devices were realized by mechanically dispersing NWs from the growth substrate to a SiO_2 (500 nm)/Si substrate (p-type, B doped) and connecting single isolated nanostructures by means of Pt electrodes (thickness of 80 nm, sputtering rate of 2 Å/s) to pre-patterned sub-millimetric probe circuits. Before metal deposition, the contact reliability was improved by an oxygen plasma treatment (40 W, 30 s). At the end of the fabrication, the sample was treated with oxygen plasma (40 W, 60 s) in order to eliminate resist residues on the NW surface. Note that the choice of Pt as the metal electrode is crucial for the realization of reliable junctions without the occurrence of interfacial oxidized layer at the metal/ZnO interface. The exposure of NWs to water-based solvents was strictly avoided during the fabrication process in order to prevent NW degradation and corrosion [27]. The NW Field Effect Transistor configuration (NW-FET) was achieved by realizing a back-gate contact to the *p*-type Si substrate through Ag paste, after etching the backside of the wafer with HF. The SiO_2 layer with thickness of 500 nm acted as the gate dielectric. Electrical measurements reported in the manuscript are acquired by considering a NW with diameter of 146 nm.

Electrical measurements were performed in a modified cryostat (Janis ST-100H) [28], connecting the sample to a cold finger inserted in a vacuum chamber (~10^{-3} mbar). The temperature of the sample was measured using a platinum resistor (Pt-100) embedded into the cold finger. In order to fix the temperature to a set-point value, a Lake-Shore 331 temperature controller coupled with a liquid-nitrogen transfer line and a heater were used. *I-V* measurements of ZnO NWs were performed using a Keithley 6430 Sub-Femtoamp SourceMeter with remote preamplifier, while the gate bias was applied using a Keithley 2410. All instruments were controlled using a Labview VI. Keithley instruments were connected to the cryostat with triaxial cables in order to minimize external noises. In addition, all electrical measurements were performed in dark conditions to avoid photo-induced carriers.

3. Results and discussion

3.1 ZnO NW characterization

The growth process by means of Vapor-Solid (VS) growth resulted in vertically aligned and hexagonal-shaped ZnO NW arrays [11] with median length and diameter of ~1.6 µm and ~100 nm, respectively (Fig. 1a) (details in Experimental Section). NWs are single crystal structures grown preferentially along the [002] crystallographic direction of wurtzite ZnO (*w*-ZnO), as confirmed by TEM measurements (Fig. 1b). The interplane distance of 2.60 Å calculated by Fast Fourier Transform (FFT) pattern, shown in the inset, corresponds to the distance between (002) planes in *w*-ZnO. As investigated in our previous works by means of X-ray Photoelectron Spectroscopy (XPS) [11,12,27], these nanostructures are characterized by high chemical purity.

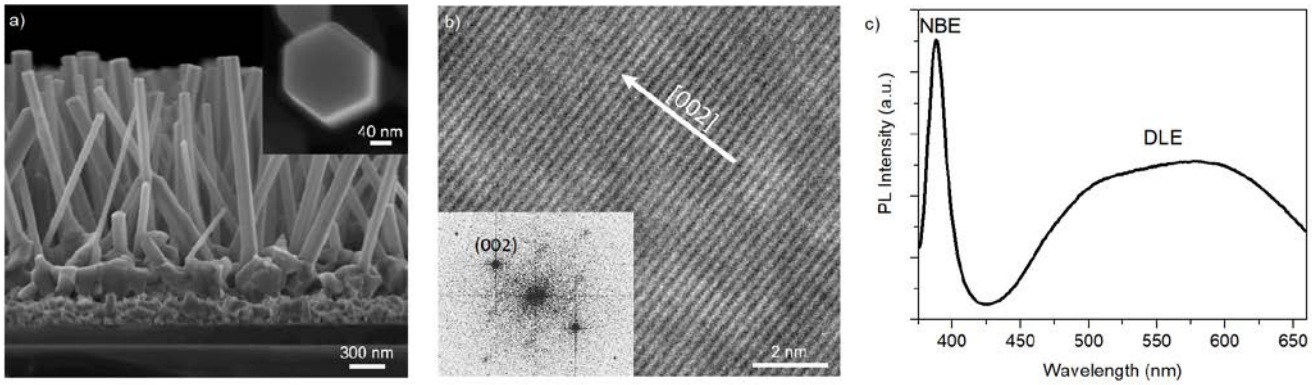

Figure 1. (a) Cross-sectional SEM image of as grown ZnO NW arrays; The inset shows a top-view of the hexagonal-shaped NW tip; (b) TEM image showing the wurtzite crystal structure of a single ZnO NW; the inset shows the Fast Fourier Transform (FFT) pattern; (c) photoluminescence spectra of as grown ZnO NWs.

Photoluminescence (PL) measurements (excitation of λ=345 nm) on as-grown ZnO NW arrays revealed the presence of a near-band-edge emission (NBE) narrow band located at 388 nm and a broader deep-level emission (DLE) band in the visible spectra region. The NBE is attributed to band-edge recombination processes of excitons while the DLE band is related to recombination process through deep levels in the ZnO band gap induced by crystal defects such as oxygen vacancies and zinc interstitials [25].

3.2 Electrical characterization and surface effects

A FE-SEM image and a schematic representation with electrical connections of a single ZnO NW contacted by Pt electrodes device are reported in Fig. 2a and b, respectively (details in Experimental Section). The highly doped Si substrate under the 500-nm-thick SiO_2 was used as a back-gate electrode for field effect measurements. As a consequence of the high surface-to-volume ratio, surface effects can strongly influence the NW conductivity, leading to the large variability of values reported in literature. Initially, in order to improve the contact quality and to desorb organic species that can be present on the NW surface, an annealing step in vacuum was performed. As reported in FIG. 2c, before annealing the NW exhibited high resistivity (Pre-1st annealing) (Fig. 2c). Subsequently, the sample was annealed in vacuum at 450 K for about 90 min. After cooling down to 300 K, the NW exhibited a linear and symmetric characteristic with enhanced conductivity (post 1st annealing). This annealing step had the result of increasing the contact quality and to remove adsorbed species on the NW surface. In order to understand the role of adsorbed species, the NW was then exposed to ambient conditions and subsequently measured in vacuum (Pre-2nd annealing), showing an increased resistivity. A new annealing (450 K, 90 min) was then necessary to desorb these chemical species on the surface, restoring the conductivity achieved after the first annealing (Post 2nd annealing).

These observations showed that adsorbed species such as oxygen and hydroxyl groups on the surface act as charge traps capturing free electrons and forming a depleted region on the NW surface [29–32] (Fig. 2d). The adsorption of these chemical species can be facilitated by the presence of surface defects that acts as adsorption sites [27]. For this reason, an increasing of the quantity of adsorbed species (i.e. increasing pressure in the vacuum chamber) results in a higher thickness of the insulating shell layer and thus in higher NW resistivity (Fig. 2e). Here, the NW resistivity was extrapolated from *I-V* characteristics that were acquired at different vacuum levels after an annealing step, starting from a pressure of $3.4 \cdot 10^{-3}$ mbar. It can be noticed that the NW resistivity increased about three times when exposed to ambient pressure.

3.3 Metal-insulator transition

The peculiar dependence of conductivity (σ) on temperature of a single ZnO NW is presented in the Arrhenius plot of Fig. 3a (details on the extrapolation of σ in Supplementary Material S1. Interestingly, the conductivity exhibited different trends as a function of temperature. At low temperatures (T < 350 K), the conductivity monotonically increases by increasing temperature, as expected for semiconductors. Instead, at high temperature (T > 400 K) the conductivity decreases by increasing temperature exhibiting a metallic-like behaviour. Considering the low temperature range (range 250 K – 81.7 K), Arrhenius plot of measured conductivity showed distinctively two slopes, suggesting that two thermally activated conduction processes are involved. As previously reported by Chiu et al. [18] and Tsai et al. [19] for temperatures below room temperature, a model based on multiple activation energies is required to describe the conduction behaviour of natively doped ZnO NWs. In our case, experimental data can be well interpolated with the following equation:

$$\sigma(T) = \frac{1}{\rho_1} e^{-\frac{E_1}{k_b T}} + \frac{1}{\rho_2} e^{-\frac{E_2}{k_b T}} \quad (1)$$

where ρ_1 and ρ_2 are temperature independent resistivity parameters, E_1 and E_2 are activation energies associated with two thermal activation processes while k_b is the Boltzmann

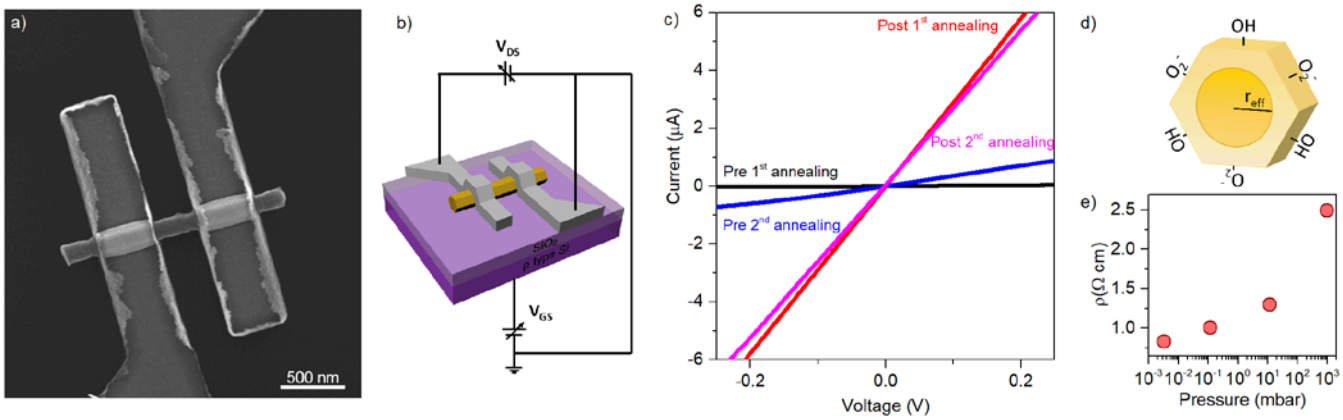

Figure 2. (a) FESEM image and (b) schematic representation with electrical connections of a single ZnO NW contacted by means of Pt electrodes. (c) effect of annealing on the *I-V* characteristic of a single ZnO NW; (d) schematic representation of the effect of adsorbed species acting as charge traps on the surface, creating an electron depleted shell region surrounding the semiconductive core of the NW; (e) effect of ambient pressure on the single ZnO NW resistivity (measurements were performed after an annealing step, by progressively filling the vacuum chamber with ambient air). Electrical measurements were performed at T = 300 K.

constant. In order to understand this peculiar behaviour, the band structure of the intrinsically doped ZnO NWs has to be considered. Despite the origin of the unintentional *n*-type doping of ZnO nanostructures is still a matter of debate, it was proposed to be related to intrinsic defects or impurities that act as shallow donors [17,33]. It is well known that, when a sufficient amount of doping is present in a semiconductor, the interaction between randomly distributed impurity states causes the formation of an impurity band [34]. Under certain conditions of doping, the impurity band can be splitted into the lower D band and the upper D^- band, arising from overlapping of ground states or negative-ion states of the impurity wave functions [35,36]. According to Chiu et al.[18], the band energy diagram of ZnO NWs (*n*-type doped) can be qualitatively represented as in Fig. 3b. The Fermi level, that is placed on the top of the D band in case of weak compensation, is expected to be placed inside the lower D band as a consequence of a slight self-compensation present in ZnO NWs, while the D^- band is generally wider than the D band [18]. In case of low temperatures (T below ~ 120 K), the low thermal energy reduces the probability for an electron to be excited from the D band to the conduction band. In this case, electrons can be thermally excited to the unoccupied states present in the D^- band and the conduction mechanism is dominated by the so-called E_2 conduction channel. Instead, by increasing temperature, the higher thermal energy increased the probability for electrons to be directly excited to the conduction band (E_1 conduction process). It has to be pointed out that we neglect a third channel of conduction arising from the nearest neighbour hopping (NNH) inside the D band since it becomes relevant for temperatures below about 20 K [18]. As reported in Fig. 3a, the model described by eq. (2) well interpolates experimental data below 250 K. The extrapolated activation energies were $E_1 = (35.1 \pm 1.2)$ meV and $E_2 = (3.8 \pm 1.4)$ meV. It has to be pointed out that the obtained values of activation energies for shallow donors here observed are in good accordance with previously reported activation energies for ZnO NWs (Supplementary Material S2). Also, the activation energy E_1 is in good accordance with the activation energy $E_a = (35 \pm 3)$ meV estimated in our previous work by considering ZnO NWs contacted by asymmetric Pt and Cu electrodes[13].

More interestingly, a metal-to-insulator transition (MIT) was observed in correspondence of the critical temperature T_c of about 365 K, as can be observed in the inset of Fig. 3a. Above this temperature, the conductivity abruptly decreased by increasing temperature, exhibiting a metallic-like behaviour. In heavily doped semiconductors, the metal-to-insulator transition can occur as a consequence of electron-electron interaction effects (Coulomb repulsion) when the carrier concentration exceeds a critical value according to the Mott criteria [22]:

$$n_c^{1/3}\, a_B^* \cong 0.25 \qquad (2)$$

where n_c is the critical carrier concentration at which the transition occurs while a_B^* is the effective Bohr radius. The effective Bohr radius can be estimated (from the equation $a_B^* = \frac{\varepsilon}{m_e^*/m_e}\, a_B$, where ε is the dielectric constant of the material and a_B is the Bohr radius) to be $a_B^* \approx 1.9$ nm in ZnO, using an effective mass of $m_e^* = 0.24\, m_e$ (m_e is the mass of the free electron) and a dielectric constant $\varepsilon = 8.66$ for wurtzite ZnO [1]. Thus, it is possible to estimate the critical carrier concentration at which the MIT occur to be $n_c \approx 2.3 \cdot 10^{18}$ cm^{-3}. However, this represents only a rough estimation of the critical carrier concentration. Indeed, it has been shown that the dielectric constant value can be strongly influenced by surface dielectric weakening effects and depends on the ZnO NW diameter [37]. Considering a dielectric constant of $\varepsilon \approx 3.5$ for a ZnO NW with diameter of 150 nm (extrapolated from Fig. 4 of ref. [37]), the effective Bohr radius and critical carrier concentration can be calculated to be $a_B^* \approx 0.8$ nm and $n_c \approx 3.0 \cdot 10^{19}$ cm^{-3}, respectively. Note that the estimation of the Bohr

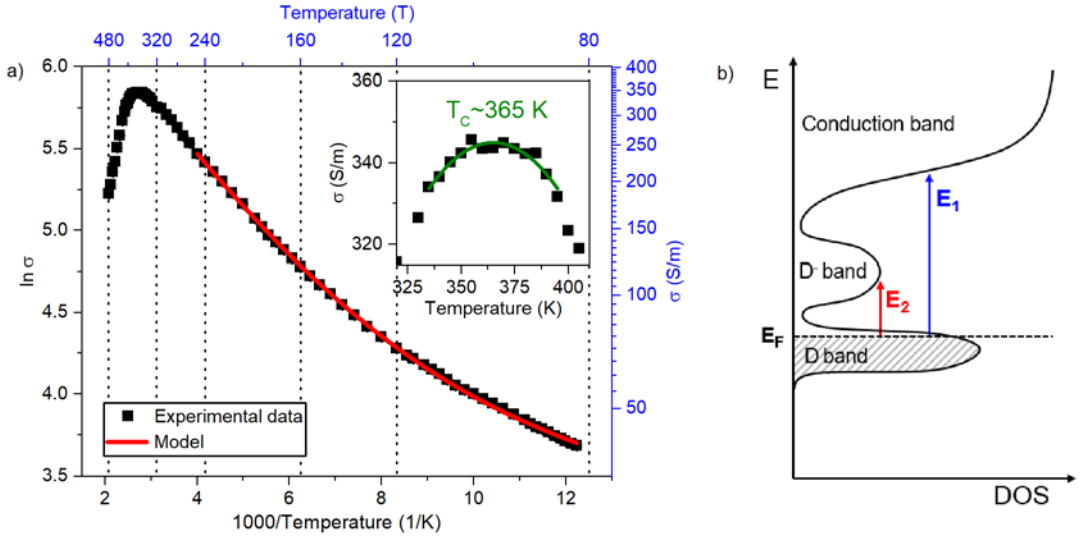

Figure 3. (a) Arrhenius plot of conductivity versus reciprocal temperature for the single ZnO NW and (b) schematic representation of the band structure.

radius in ZnO can exclude the change of the electronic structure of the material due to quantum confinement effects, being the diameter of the NW about two orders of magnitude larger than the calculated Bohr radius

As recently discussed by Chung et al. [38], the investigation of the metal-to-insulator transition is usually accompanied by structural phase change of the involved material that makes difficult a disentanglement of electronic and structural effects underlaying the transition events. However, structural changes of the wurtzite crystalline structure of the ZnO NW can be safely excluded in our case, since the temperature range adopted for electrical measurements is well below the synthesis temperature (650°C) of these nanostructures. As far as we know, metal-to-insulator transition in natively doped single ZnO NWs was previously reported only below room temperature or by applying external stimuli such as illumination. Indeed, a metal-to-insulator transition in single ZnO NWs was reported by Modepalli et al. [25] at about 250 K, while Chang et al. [26] observed a transition temperature of about 210 K but only after continuous UV irradiation for enhancing the charge carrier density through photoexcitation. An UV induced transition was reported also in case of single Ga-doped ZnO NW [39] and SnO_2 nanobelt [40].

3.3 Charge density and mobility

In order to thoroughly investigate the electronic properties of these nanostructures, field effect measurements in NW-FET configuration were performed. I_{DS} versus V_{DS} curves acquired in vacuum at room temperature for different gate bias voltages exhibited good linearity over a large gate bias range (+50/-50 V) (Fig. 4a). In addition, I_{DS} versus V_{GS} curves (transconductance curves) for different drain-source bias are reported in Fig. 4b. Both I_{DS}-V_{DS} and I_{DS}-V_{GS} curves evidenced a typical *n*-type FET behaviour, showing a decrease of the NW conductance by decreasing the gate bias voltage. Note that the annealing step before measurements is crucial since adsorbed species were observed to have a strong impact on the electrostatic gating effect (Supplementary material S3).

The dependence of the transconductance behaviour on temperature was investigated in the range 360 K – 81.6 K (Fig. 4c). From transconductance measurements it was possible to estimate charge carrier density and mobility. Charge density (n) in the channel was extrapolated according to the equation [8]:

$$n \approx \frac{C_{NW} V_{th}}{q \pi r^2 L} \quad (3)$$

where gate capacitance (C_{NW}) was estimated (assuming a cylinder-on-plate model) from the relation [41]:

$$C_{\mathrm{NW}} \approx \frac{2 \pi \varepsilon_0 \varepsilon_r L}{cosh^{-1}\left(\frac{r+d_{ox}}{r}\right)} \quad (4)$$

and V_{th} was the threshold voltage (calculated by linear interpolation of the I_{DS} versus V_{GS} curve and I=0), q is the fundamental charge, r is the NW radius (r = 73 nm), L is the distance between electrodes (L = 350 nm), ε_0 the vacuum permittivity, ε_r was the relative permittivity of SiO_2 (ε_r =3.9) while d_{ox} is the gate oxide thickness (d_{ox} = 500 nm). Mobility was estimated according to the following relation [41]:

$$\mu \approx \frac{dI_{SD}}{dV_G} \cdot \frac{L^2}{C_{\mathrm{NW}} V_{DS}} \quad (5)$$

Charge density and mobility as a function of temperature are reported in Fig. 5a and b, respectively.

A carrier density of about $5.8 \cdot 10^{18}$ cm^{-3} was estimated at room temperature. Considering the charge density dependence on temperature, it can be noticed that the ZnO NW exhibited

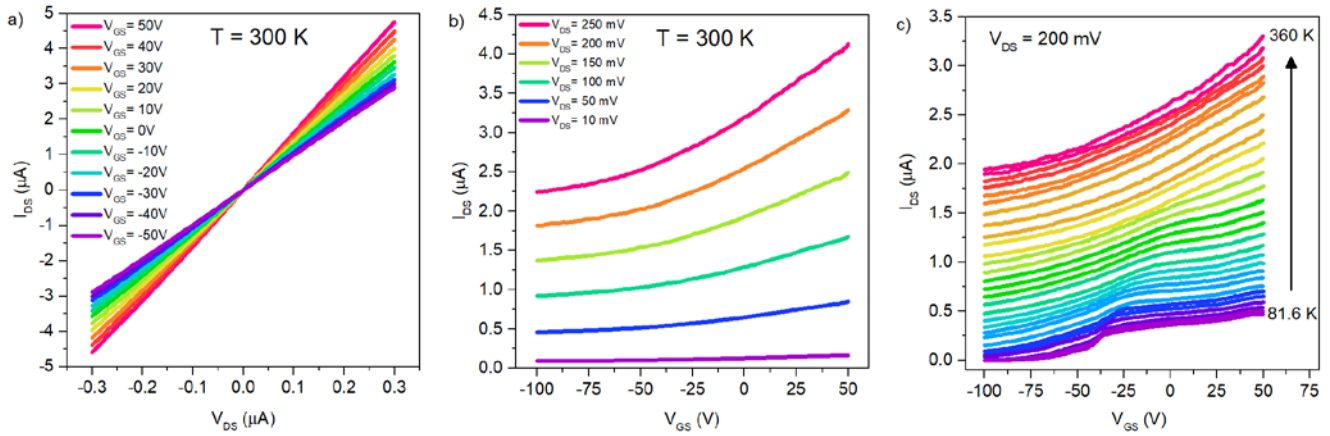

Figure 4. Field-effect measurements. (a) I_{DS} versus V_{DS} curves for different back gate voltage bias and (b) transconductance curves (I_{DS} versus V_{GS} curves) acquired for different drain-source bias; measurements were performed at a fixed temperature of 300 K; (c) transconductance curves acquired in the temperature range 81.6 K – 360 K with a constant V_{DS} of 200 mV.

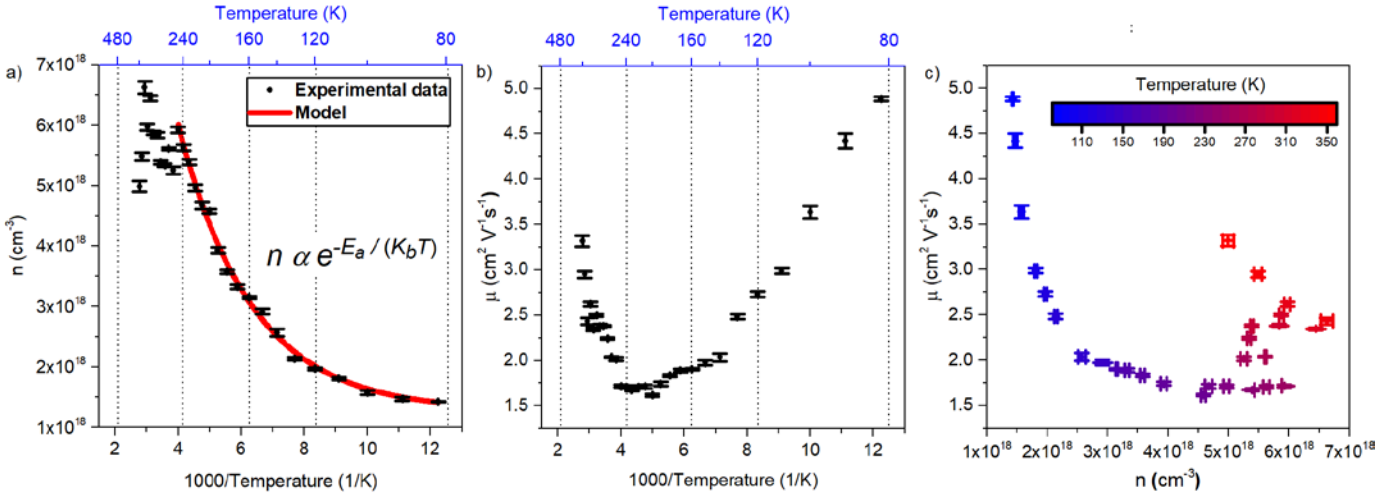

Figure 5. Arrhenius plot of a) charge density and b) field effect mobility as a function of temperature; c) field effect mobility as a function of charge density where the color of scattered points represents the temperature.

an exponential behaviour versus reciprocal temperature ($n \propto e^{-E_{a1}/k_bT}$) below 250 K, where the activation energy E_{a1} was calculated to be (36.9 ± 1.3) meV from the best fit. This value of activation energy is in good agreement with the previously reported activation energy E_1 related to the energy required for an electron to be promoted from the D band to the conduction band, while an estimation of the activation energy E_2 is hampered in this experimental configuration. This value of activation energy was extrapolated from measurements that are completely independent from previously discussed *I-V-T* measurements, confirming the consistency of experimental results.

In case of carrier mobility, a maximum value of about 4.9 cm^2 V^{-1}s^{-1} was measured at 81.6 K. Increasing temperature, the mobility decreased and reached a minimum of about 1.7 cm^2 V^{-1}s^{-1} in the range 200 K – 250 K. Further increasing the temperature over about 250 K, the mobility started again to increase and reached a value of about 3.3 cm^2 V^{-1}s^{-1} at 360 K. The relationship between mobility and carrier density is presented in Fig. 5c, where it is possible to notice that mobility decreases as the carrier concentration increase. However, when the carrier concentration reaches the value of about $6 \cdot 10^{18}$ cm^{-3} the conductivity dependence on temperature can be mainly attributed to the increase of the electron mobility rather than an increase of the carrier density that remained nearly constant by increasing temperature.

It has to be remarked that the charge concentration in the range of $5\text{-}7 \cdot 10^{18}$ cm^{-3} observed for temperatures just below the critical temperature fall qualitatively in the range of critical carrier concentration required for the MIT transition, as previously discussed. Also, the not clear dependence on temperature of carrier density by approaching the MIT critical temperature can be tentatively attributable to a nearly complete ionization of donor impurities, even if this aspect still needs further investigation.

3. Conclusion

In conclusion, we have investigated the metal-insulator transition and electronic transport in single crystalline ZnO NWs grown by CVD and characterized by high crystal quality. As revealed by temperature-dependent electrical measurements, in the temperature range 81.7 K-250 K the electronic transport can be well described by means of a two thermally activated conduction mechanism. Interestingly, it was reported that it is possible to tune the electrical behavior of these nanostructures from semiconducting to metallic as a function of temperature. The crossover temperature of the metal-to-insulator transition was observed to be ~365 K. Field-effect measurements revealed that the peculiar electronic properties of the ZnO NWs are attributable to the high intrinsic *n*-type doping of these nanostructures where the carrier concentration was estimated to be $5.8 \cdot 10^{18}$ cm^{-3} at room temperature, just below the critical carrier concentration for the metal-to-insulator transition.

Acknowledgements

The support of Mauro Raimondo for SEM is gratefully acknowledged. Part of this work has been carried out at Nanofacility INRiM, a laboratory supported by the Compagnia di San Paolo Foundation. The authors declare no competing financial or non-financial interests. The data that support the findings of this study are available from the authors on reasonable request.

References

[1] Fan Z and Lu J G 2005 Zinc Oxide Nanostructures: Synthesis and Properties *J. Nanosci. Nanotechnol.* **5** 1561–73

[2] Yan R, Gargas D and Yang P 2009 Nanowire photonics *Nat. Photonics* **3** 569–76

[3] Sidiropoulos T P H, Röder R, Geburt S, Hess O, Maier S A, Ronning C and Oulton R F 2014 Ultrafast plasmonic nanowire lasers near the surface plasmon frequency *Nat. Phys.* **10** 870–6

[4] Wen B, Sader J E and Boland J J 2008 Mechanical Properties of ZnO Nanowires *Phys. Rev. Lett.* **101** 175502

[5] Wang X, Zhou J, Song J, Liu J, Xu N and Wang Z L 2006 Piezoelectric Field Effect Transistor and Nanoforce Sensor Based on a Single ZnO Nanowire *Nano Lett.* **6** 2768–72

[6] Wan Q, Li Q H, Chen Y J, Wang T H, He X L, Li J P and Lin C L 2004 Fabrication and ethanol sensing characteristics of ZnO nanowire gas sensors *Appl. Phys. Lett.* **84** 3654–6

[7] Choi A, Kim K, Jung H-I and Lee S Y 2010 ZnO nanowire biosensors for detection of biomolecular interactions in enhancement mode *Sensors Actuators B Chem.* **148** 577–82

[8] Goldberger J, Sirbuly D J, Law M and Yang P 2005 ZnO Nanowire Transistors *J. Phys. Chem. B* **109** 9–14

[9] Chang P and Lu J G 2008 ZnO Nanowire Field-Effect Transistors *IEEE Trans. Electron Devices* **55** 2977–87

[10] Long J, Xiong W, Wei C, Lu C, Wang R, Deng C, Liu H, Fan X, Jiao B, Gao S and Deng L 2020 Directional Assembly of ZnO Nanowires via Three-Dimensional Laser Direct Writing *Nano Lett.* acs.nanolett.0c01378

[11] Milano G, Porro S, Ali M Y, Bejtka K, Bianco S, Beccaria F, Chiolerio A, Pirri C F and Ricciardi C 2018 Unravelling Resistive Switching Mechanism in ZnO NW Arrays: The Role of the Polycrystalline Base Layer *J. Phys. Chem. C* **122** 866–74

[12] Milano G, Luebben M, Ma Z, Dunin-Borkowski R, Boarino L, Pirri C F, Waser R, Ricciardi C and Valov I 2018 Self-limited single nanowire systems combining all-in-one memristive and neuromorphic functionalities *Nat. Commun.* **9** 5151

[13] Milano G, Boarino L and Ricciardi C 2019 Junction properties of single ZnO nanowires with asymmetrical Pt and Cu contacts *Nanotechnology* **30** 244001

[14] Porro S, Risplendi F, Cicero G, Bejtka K, Milano G, Rivolo P, Jasmin A, Chiolerio A, Pirri C F and Ricciardi C 2017 Multiple resistive switching in core–shell ZnO nanowires exhibiting tunable surface states *J. Mater. Chem. C* **5** 10517–23

[15] Milano G, Porro S, Valov I and Ricciardi C 2019 Recent Developments and Perspectives for Memristive Devices Based on Metal Oxide Nanowires *Adv. Electron. Mater.* **5** 1800909

[16] Miranda E, Milano G and Ricciardi C 2020 Modeling of Short-Term Synaptic Plasticity Effects in ZnO Nanowire-Based Memristors Using a Potentiation-Depression Rate Balance Equation *IEEE Trans. Nanotechnol.* **19** 609–12

[17] Janotti A and Van de Walle C G 2009 Fundamentals of zinc oxide as a semiconductor *Reports Prog. Phys.* **72** 126501

[18] Chiu S-P, Lin Y-H and Lin J-J 2009 Electrical conduction mechanisms in natively doped ZnO nanowires *Nanotechnology* **20** 015203

[19] Tsai L-T, Chiu S-P, Lu J G and Lin J-J 2010 Electrical conduction mechanisms in natively doped ZnO nanowires (II) *Nanotechnology* **21** 145202

[20] Stiller M, Barzola-Quiquia J, Zoraghi M and Esquinazi P 2015 Electrical properties of ZnO single nanowires *Nanotechnology* **26** 395703

[21] Ma Y-J, Zhang Z, Zhou F, Lu L, Jin A and Gu C 2005 Hopping conduction in single ZnO nanowires *Nanotechnology* **16** 746–9

[22] MOTT N F 1968 Metal-Insulator Transition *Rev. Mod. Phys.* **40** 677–83

[23] Imada M, Fujimori A and Tokura Y 1998 Metal-insulator transitions *Rev. Mod. Phys.* **70** 1039–263

[24] Yang Z, Ko C and Ramanathan S 2011 Oxide Electronics Utilizing Ultrafast Metal-Insulator Transitions *Annu. Rev. Mater. Res.* **41** 337–67

[25] Modepalli V, Jin M-J, Park J, Jo J, Kim J-H, Baik J M, Seo C, Kim J and Yoo J-W 2016 Gate-Tunable Spin Exchange Interactions and Inversion of Magnetoresistance in Single Ferromagnetic ZnO Nanowires *ACS Nano* **10** 4618–26

[26] Chang P-C and Lu J G 2008 Temperature dependent conduction and UV induced metal-to-insulator transition in ZnO nanowires *Appl. Phys. Lett.* **92** 212113

[27] Milano G, D'Ortenzi L, Bejtka K, Mandrile L, Giovannozzi A M, Boarino L, Pirri C F, Ricciardi C and Porro S 2018 Tuning ZnO Nanowire Dissolution by Electron Beam Modification of Surface Wetting Properties *J. Phys. Chem. C* **122** 8011–21

[28] Cultrera A, Amato G, Boarino L and Lamberti C 2014 A modified cryostat for photo-electrical characterization of porous materials in controlled atmosphere at very low gas dosage *AIP Adv.* **4** 087134
[29] Liao Z-M, Liu K-J, Zhang J-M, Xu J and Yu D-P 2007 Effect of surface states on electron transport in individual ZnO nanowires *Phys. Lett. A* **367** 207–10
[30] Chen C-Y, Retamal J R D, Wu I-W, Lien D-H, Chen M-W, Ding Y, Chueh Y-L, Wu C-I and He J-H 2012 Probing Surface Band Bending of Surface-Engineered Metal Oxide Nanowires *ACS Nano* **6** 9366–72
[31] Milano G, Luebben M, Laurenti M, Porro S, Bejtka K, Bianco S, Breuer U, Boarino L, Valov I and Ricciardi C 2019 Ionic Modulation of Electrical Conductivity of ZnO Due to Ambient Moisture *Adv. Mater. Interfaces* **6** 1900803
[32] Milano G, Raffone F, Luebben M, Boarino L, Cicero G, Valov I and Ricciardi C 2020 Water-Mediated Ionic Migration in Memristive Nanowires with a Tunable Resistive Switching Mechanism *ACS Appl. Mater. Interfaces* acsami.0c13020
[33] Liu L, Mei Z, Tang A, Azarov A, Kuznetsov A, Xue Q-K and Du X 2016 Oxygen vacancies: The origin of <math> <mi>n</mi> </math> -type conductivity in ZnO *Phys. Rev. B* **93** 235305
[34] Hung C S and Gliessman J R 1954 Resistivity and Hall Effect of Germanium at Low Temperatures *Phys. Rev.* **96** 1226–36
[35] Nishimura H 1965 Impurity Conduction in the Intermediate Concentration Region *Phys. Rev.* **138** A815–21
[36] Norton P 1976 Formation of the Upper Hubbard Band from Negative-Donor-Ion States in Silicon *Phys. Rev. Lett.* **37** 164–8
[37] Yang Y, Guo W, Wang X, Wang Z, Qi J and Zhang Y 2012 Size Dependence of Dielectric Constant in a Single Pencil-Like ZnO Nanowire *Nano Lett.* **12** 1919–22
[38] Lee D, Chung B, Shi Y, Kim G-Y, Campbell N, Xue F, Song K, Choi S-Y, Podkaminer J P, Kim T H, Ryan P J, Kim J-W, Paudel T R, Kang J-H, Spinuzzi J W, Tenne D A, Tsymbal E Y, Rzchowski M S, Chen L Q, Lee J and Eom C B 2018 Isostructural metal-insulator transition in VO 2 *Science (80-.).* **362** 1037–40
[39] Li D, Zhao L, Wu R, Ronning C and Lu J G 2011 Temperature-dependent photoconductance of heavily doped ZnO nanowires *Nano Res.* **4** 1110–6
[40] Viana E R, Ribeiro G M, de Oliveira A G and González J C 2017 Metal-to-insulator transition induced by UV illumination in a single SnO 2 nanobelt *Nanotechnology* **28** 445703
[41] Opoku C, Dahiya A S, Cayrel F, Poulin-Vittrant G, Alquier D and Camara N 2015 Fabrication of field-effect transistors and functional nanogenerators using hydrothermally grown ZnO nanowires *RSC Adv.* **5** 69925–31